Available online at www.sciencedirect.com
ScienceDirect
Trans. Nonferrous Met. Soc. China 31(2021) 331−344
Transactions of Nonferrous Metals Society of China
www.tnmsc.cn

Microstructures and mechanical properties of in-situ TiB_2/Al−*x*Si−0.3Mg composites

Yu-xuan LIU[1], Ri-chu WANG[1,2], Chao-qun PENG[1],
Zhi-yong CAI[1,2], Zhao-hui ZHOU[3], Xiao-geng LI[3], Xuan-yang CAO[3]

1. School of Materials Science and Engineering, Central South University, Changsha 410083, China;
2. National Key Laboratory of Light High Strength Structural Materials,
Central South University, Changsha 410083, China;
3. Changsha Advanced Materials Industrial Research Institute, Changsha 410000, China

Received 16 March 2020; accepted 18 December 2020

Abstract: In-situ 2 vol.% TiB_2 particle reinforced Al−*x*Si−0.3Mg (*x*=7, 9, 12, 15 wt.%) composites were prepared by the salt−metal reaction, and the microstructures and mechanical properties were investigated. The results show that the TiB_2 particles with a diameter of 20−80 nm and the eutectic Si with a length of 1−10 μm are the main strengthening phases in the TiB_2/Al−*x*Si−0.3Mg composites. The TiB_2 particles promote grain refinement and modify the eutectic Si from needle-like to short-rod shape. However, the strengthening effect of TiB_2 particles is weakened as the Si content exceeds the eutectic composition, which can be attributed to the formation of large and irregular primary Si. The axial tensile test results and fractography observations indicate that these composites show more brittle fracture characteristics than the corresponding alloy matrixes.

Key words: Al−Si alloy; in-situ reaction; aluminum matrix composite; microstructure; mechanical properties

1 Introduction

Al−Si alloys exhibiting good corrosion and wear resistance, high thermal conductivity, and low thermal expansion coefficient are widely used in aerospace, transportation, electronic components, and other fields [1,2]. However, extensive growth of primary and eutectic Si phases is inevitable in the traditional cast Al−Si alloys due to the low cooling rate, especially in the alloys with high Si content [3].

The modification of Si phases has widely been studied for decades. Many elements were reported as modifiers for Al−Si alloy, such as Sc [4], Sm [5], Sr [6], P [7], and Y [8]. It was also reported that the Si phases could be refined remarkably by the addition of stable fine particles, similar to the effect of modifiers, and then the mechanical properties and wear resistance were enhanced [9]. The stable particles could restrict grain growth by pinning grain boundaries. Additionally, the stable particles are usually immutable hard phase, which can improve the strength of the material by blocking the dislocation movement and the corrosion resistance [10], the wear resistance [11], and the high-temperature performance [12]. LLOYD [13] reported that SiC particles reacted with liquid Al and formed an Al_4C_3 layer at the reinforcement−matrix interface, which reduced the mechanical properties of the composites, especially at high temperatures. In the Al−Mg matrix composites, Al_2MgO_4 is always formed by the reaction between Mg and Al_2O_3 reinforcement. The existence of

Corresponding author: Zhi-yong CAI; Tel: +86-731-88836638; E-mail: zycaimse@163.com
DOI: 10.1016/S1003-6326(21)65499-7

Al_2MgO_4 makes it impossible to form a good interface bonding in the composites, leading to a detrimental effect on mechanical properties [14]. In contrast, TiB_2 particles are thermo-dynamically stable in liquid Al [15,16]. Furthermore, the stability of TiB_2 permits the application of a wide range of solid- and liquid-state processing techniques for preparing particle reinforced metal matrix composites (PMMCs). Therefore, TiB_2 is a fantastic reinforcing phase for hyper-/hypo-eutectic Al−Si alloys [17−19], considering its high melting point, high hardness, high elastic modulus, and good electrical conductivity.

Generally, metal matrix composites are prepared by the addition (ex-situ) method and the in-situ method [17−22]. Compared with the traditional ex-situ method, the in-situ method introduces one or more reinforcements in a matrix by chemical reactions under certain conditions [23]. The in-situ method has the following characteristics. (1) The reinforcements are thermo-dynamically stable, which nucleate and grow in the metal melt. Therefore, the surface of the reinforcements is clean, which avoids the problem of low compatibility with the matrix, and high interfacial bonding strength is obtained [24]. (2) The type, size, distribution, and quantity of in-situ reinforcements can be effectively controlled by selecting the type, composition, and reactivity of reaction elements or compounds. (3) Processes such as synthesis, treatment, and addition of reinforcements are omitted. Consequently, the in-situ forming process is simple and effective. (4) The in-situ formation of reinforcements from liquid metal matrix can fabricate net-shape components with complex shapes and large sizes by casting. (5) The strength and elastic modulus of the material can be significantly improved while the material has good toughness and high-temperature properties [25]. (6) The particles of the reinforcements are small and uniformly distributed in the matrix. Therefore, the in-situ formed composites possess excellent mechanical properties [21,26,27].

However, the in-situ TiB_2 particles tend to co-exist with the second phase during solidification. The accumulation of TiB_2 particles can be explained from the crystallographic point of view. During the solidification process, the high concentration of the surrounding particles results in the impulse on TiB_2 particles, which hinders the rotation and prevents them from moving in a more advantageous crystal direction. VIVEKANANDA et al [28] studied the effect of aluminothermic reduction parameters on the grain refinement of in-situ TiB_2/Al composites. The reaction was completed under higher holding time (40 min) and adding time (20 min), resulting in the finer TiB_2 particles, which had a better effect on the grain refinement. JAVADI et al [29] reported a preparation method of effectively combining TiB_2 nano-particles into Al matrix by flux assisted liquid-phase treatment. The Al−30vol.%TiB_2 nanocomposites prepared by this method have a microhardness of HV (485.9±16.9). RAJAN et al [30] prepared *x*wt.%TiB_2/AA7075 composites by the in-situ reaction of K_2TiF_6 and KBF_4 in molten Al. The results showed that the in-situ TiB_2 particles were characterized with uniform distribution, clear interface, excellent bonding, and various shapes such as cubic, spherical, and hexagonal. The microhardness and ultimate tensile strength (UTS) of the composites were enhanced. It was also found that friction stir processing (FSP) could enhance the distribution of TiB_2 particles in the composites because they were fragmented and rounded due to the abrading action of the rotating tool [31]. FENG and FROYEN [32] found that TiB_2 particles prepared by the mixed salt−metal reaction of K_2TiF_6 and KBF_4 usually show clusters in pure Al matrix composites. The dispersion of TiB_2 particles in Al can be improved by adding Si into the matrix. Simultaneously, using Al−Si alloy with low Si content (2% or 5%) as matrix cannot effectively improve the dispersion of TiB_2 particles.

According to the results of FENG and FROYEN [32], more TiB_2 particles were pushed by the solidification front to the interfaces of solid−liquid Al in the eutectic Al−Si alloy. Compared with the solidification of the single-phase primary crystal, TiB_2 particles in the eutectic solidification are well-distributed. Therefore, it is important to clarify the interaction between the in-situ TiB_2 particles and the Al−Si alloys containing various Si contents. In this work, hypo-eutectic, eutectic, and hyper-eutectic Al−Si alloys with Si contents of 7, 9, 12 and 15 wt.% were chosen. Considering the machinability and maneuverability of the composite, the Si content should not be over 15 wt.%. Additionally, introducing a small amount of Mg can effectively

improve the strength due to the Al−Mg solutions. In-situ TiB_2/Al−xSi−0.3Mg (x=7, 9, 12, 15 wt.%) composites were synthesized by the salt−metal reaction and the effects of TiB_2 particles on the microstructure and mechanical properties of the 2vol.%TiB_2/Al−xSi−0.3Mg composites were investigated.

2 Experimental

2.1 Materials preparation

Al−xSi−0.3Mg (x=7, 9, 12, 15 wt.%) alloys and in-situ 2 vol.% TiB_2 reinforced Al−xSi−0.3Mg composites were prepared. The in-situ composites were fabricated by the salt−metal reaction method. Firstly, pure Al (99.95%) and Al−60Si master alloy were melted at 720 °C and degassed with C_2Cl_6 as a deaerator. After degassing, the melt was heated to 850 °C and held for 5 min. Secondly, the pre-mixed K_2TiF_6 and KBF_4 (analytical grade) powders with Ti/B molar ratio of 1:2 were added to the melt. The additions of KBF_4 and K_2TiF_6 added per 1000 g matrix alloy were 42.9 and 40.8 g, respectively. The calculation formulas are as follows:

$$n(TiB_2)=\frac{m(\text{Matrix})}{\rho(\text{Matrix})}\times\frac{2}{98}/(4.52\times69.5) \quad (1)$$

$$n(KBF_4)=n(TiB_2)\times2\times126 \quad (2)$$

$$m(K_2TiF_6)=n(TiB_2)\times240 \quad (3)$$

where n represents the amount of substance, m represents the mass, and ρ represents the density. In the process of adding mixed salt, a vane stirrer was used to prevent the agglomeration of the mixed powder from causing uneven distribution of TiB_2. The reaction was held for 20 min until no smoke came out. Thirdly, after the powder was added to the melt, the melt was continuously stirred for 20 min and allowed to stay for 20 min to complete the reaction. The pure Mg blocks covered with Al foil were added to the melt at 720 °C. Finally, the residual salt was removed, and the melt was cast into a 25 mm × 100 mm × 150 mm iron mold. The smelting device used in the experiment is shown in Fig. 1.

2.2 Characterization

Six samples were taken from different parts of each TiB_2/Al−7Si−0.3Mg composite and Al−7Si−0.3Mg alloy. The density was measured by drainage method, and the porosity was calculated by the average value.

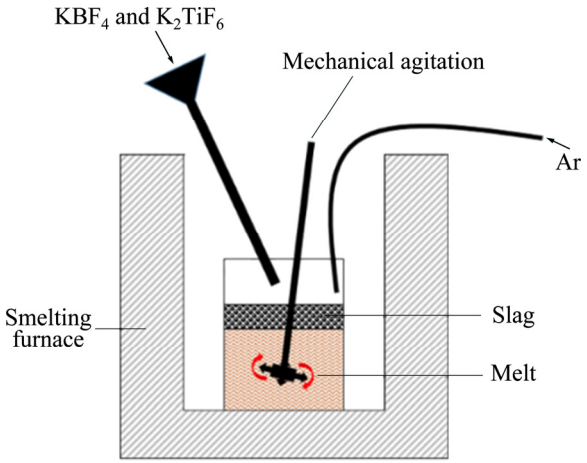

Fig. 1 Schematic diagram of smelting device for salt−metal reaction

Characteristics of the in-situ formed TiB_2 particles were observed using electron probe microanalysis (EPMA, JXA−8230, Japan) and field emission scanning electron microscope (FE-SEM, Sirion 200, America) outfitted with energy-dispersive spectroscopy (EDS) detector. The morphology and distribution of the TiB_2 particles were observed using metallographic microscope (POLYVAR-MET, Denmark), scanning electron microscope (SEM, Quanta−200, Holland), and the particle size was measured using ImageJ software with the SEM images.

The microstructures of the Al−xSi−0.3Mg alloys and the TiB_2/Al−xSi−0.3Mg composites were characterized by SEM and TEM. SEM samples were prepared by mechanical polishing, and the TEM samples were prepared by ion-beam thinning. The interface between the TiB_2 particle and the Al matrix was observed using a bright-field image of TEM. The interface region and the adjacent matrix structure micro-regions were detected by electron diffraction.

2.3 Tensile tests

Tensile tests of the Al−xSi−0.3Mg alloys and the TiB_2/Al−xSi−0.3Mg composites were carried out using a materials testing system (MTS LANDMARK, America) at room temperature (RT). The tensile tests were implemented at a constant strain rate of 1.0 mm/min, according to the GB/T228.1—2010 standard. The tensile strength and elongation of each sample were both average

values of three measurements under the same condition. Tensile fracture surfaces were observed using SEM.

3 Results and discussion

3.1 Salt−metal reaction to form TiB_2 particles

Figure 2 shows the XRD patterns of the as-cast Al−7Si−0.3Mg alloy and the in-situ TiB_2/Al−7Si−0.3Mg composite.

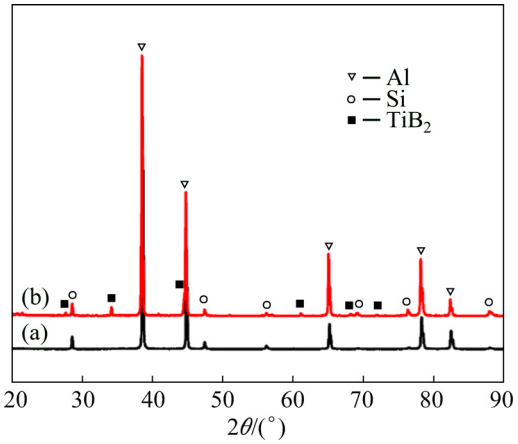

Fig. 2 XRD patterns of as-cast Al−7Si−0.3Mg alloy (a) and in-situ TiB_2/Al−7Si−0.3Mg composite (b) showing formation of TiB_2 particles

In comparison with the Al−7Si−0.3Mg alloy, only TiB_2 phase is observed in the composite. The absence of brittle phases (e.g. Al_3Ti) suggests that they are significantly suppressed during the salt−metal reaction, or the amount is less than 1%. After adding the mixed salt (K_2TiF_6 and KBF_4), the following reactions occur at high temperature [33]:

$$3K_2TiF_6+13Al=3Al_3Ti+3KAlF_4+K_3AlF_6 \quad (4)$$

$$2KBF_4+3Al=AlB_2+2KAlF_4 \quad (5)$$

$$Al_3Ti+AlB_2=TiB_2+4Al \quad (6)$$

The overall reaction can be expressed in the following reaction:

$$6KBF_4+3K_2TiF_6+10Al=9KAlF_4+K_3AlF_6+3TiB_2 \quad (7)$$

In Reaction (7), K_3AlF_6 and $KAlF_4$ will escape in the form of liquid and gas or exist in melt in the form of slag, thus forming an Al−Si−Ti−B system. Since the activity of Al is higher than that of Si, the Al−Si−Ti−B quaternary system transforms into the Al−Ti−B ternary system. In this system, the possible reaction products are TiB_2, Al_3Ti, and AlB_2.

$$[Ti]+2[B]=TiB_2(s) \quad (8)$$

$$3Al(l)+[Ti]=Al_3Ti(s) \quad (9)$$

$$Al(l)+2[B]=AlB_2(s) \quad (10)$$

where [Ti] represents the dissolved Ti in the melt, and [B] represents the dissolved B in the melt.

To study the probability of Al−Ti−B reactions, the Gibbs free energy changes (ΔG) in the reactions for 1 mol reactants were calculated based on thermodynamic data [34]. The Gibbs free energy changes $\Delta G_{A_xB_y}$ of the three products are given by

$$\Delta G_{A_xB_y}=\Delta H-T\Delta S \quad (11)$$

where ΔH is the enthalpy change of the product A_xB_y at temperature T, and ΔS is the standard entropy. Table 1 shows the calculated values of enthalpy, entropy and Gibbs free energy changes of products at 850 °C.

Table 1 Calculated values of enthalpy, entropy and Gibbs free energy changes of products at 850 °C

Product	ΔH/ (J·mol^{-1})	ΔS/ (J·mol^{-1}·K^{-1})	ΔG/ (J·mol^{-1})
Al_3Ti	90198	143.913	−114735
AlB_2	53488	82.183	−140614
TiB_2	53983	83.379	−306303

It is seen from Table 1 that TiB_2 is the easiest to form in the melt because it has the lowest Gibbs free energy change, and its forming ability is the strongest. Therefore, TiB_2 will form preferentially when the mixed salt of KBF_4 and K_2TiF_6 is added to the molten Al−Si alloy solution at 850 °C. Additionally, it can be seen from Eq. (4) that if the content of [Ti] is excessive, the reaction will be able to produce Al_3Ti particles. However, it will continue to react with AlB_2 to form TiB_2 due to the thermodynamic instability of Al_3Ti. Therefore, the Ti/B molar ratio should be strictly controlled when the mixed salt of KBF_4 and K_2TiF_6 is added to avoid the formation of harmful phases Al_3Ti and AlB_2.

3.2 Microstructure and mechanical properties of Al−7Si−0.3Mg alloy and TiB_2/Al−7Si−0.3Mg composite

Microstructures of the Al−7Si−0.3Mg alloy and the in-situ TiB_2/Al−7Si−0.3Mg composite are shown in Fig. 3. Figures 3(a) and (b) exhibit the

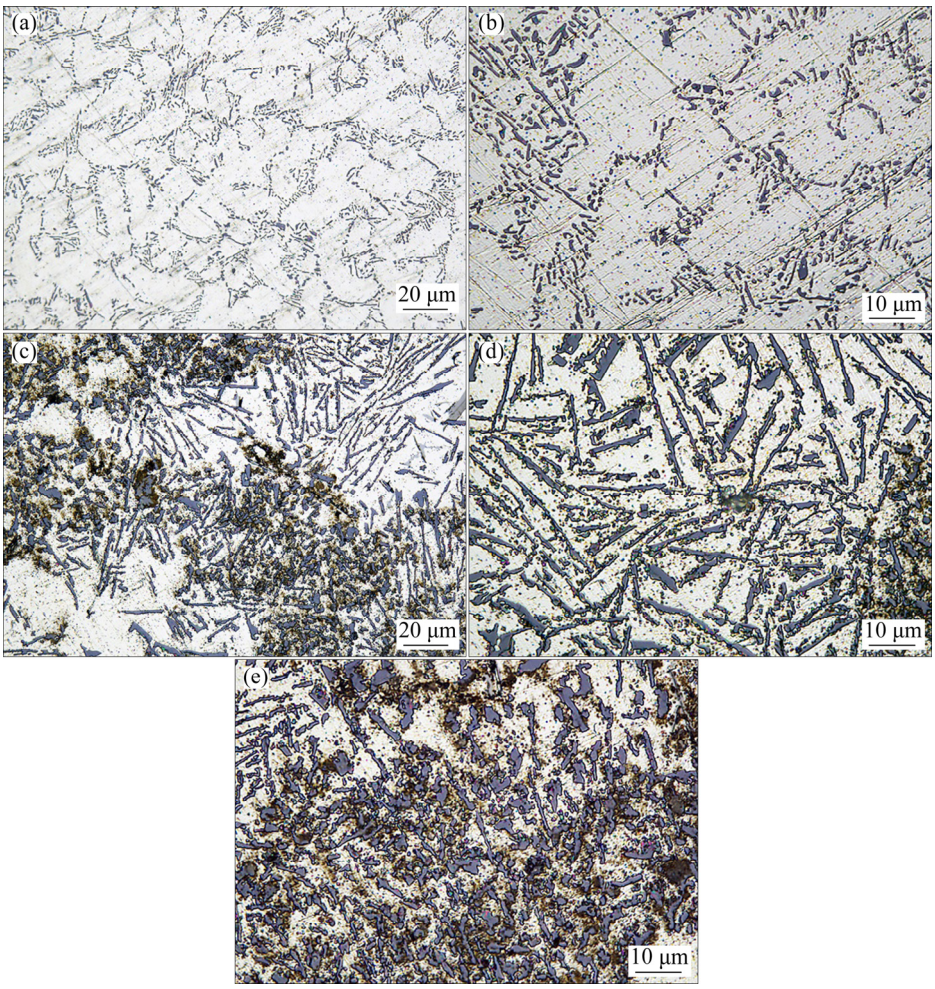

Fig. 3 Metallographic microstructures of Al−7Si−0.3Mg alloy (a, b) and in-situ TiB_2/Al−7Si−0.3Mg composite (c−e)

metallographic microstructures of the alloy enlarged 500 times and 1000 times, respectively. It is seen that the dendritic α(Al) and acicular eutectic Si in the Al−Si alloy are located at the grain boundaries. Figures 3(c−e) show the microstructures of the TiB_2/Al−7Si−0.3Mg composite at different multiples. It is seen from Fig. 3(c) that the clusters of the TiB_2 particles have different metallographic structures from those without TiB_2. Figure 3(d) shows the "non-TiB_2" area of TiB_2/Al−0.7−Si−0.3Mg composite, which is caused by the localized distribution of TiB_2 and shows a typical dendritic eutectic Si. In Fig. 3(e), the brown dispersed particles are TiB_2, which are distributed evenly in the agglomeration area. Therefore, the size of eutectic Si is refined, and the morphology of eutectic Si transforms into an equiaxed shape after introducing the in-situ TiB_2 particles.

Secondary electron (SE) micrographs of the Al−7Si−0.3Mg alloy and the TiB_2/Al−7Si−0.3Mg composite after being etched by Keller's reagent (2.5% HNO_3 + 1.5% HCl + 1% HF + 95% H_2O, volume fraction) are shown in Fig. 4. The morphology of TiB_2 particles in the composite has a hexagonal or cuboid shape, which is related to the preferential adsorption of Si on $(10\bar{1}1)$, $(11\bar{2}0)$, and $(1\bar{2}12)$ crystal faces. Figure 4(b) reveals a low magnification SEM image of the TiB_2/Al−7Si−0.3Mg composite, which shows the general nature of the distribution of TiB_2. Most of the TiB_2 particles are distributed at the grain boundaries. There are some regional clusters of TiB_2, which are marked by the red circle. As seen from Fig. 4(c), the eutectic Si is adjacent to the Al dendrites. The eutectic Si phase usually appears as the acicular shape with a length of 1−10 μm. In Fig. 4(d), the TiB_2 particles tend to co-exist with eutectic Si at the grain boundaries and have a certain degree of agglomeration in the micro-regions. The agglomeration of in-situ TiB_2 particles is typical in

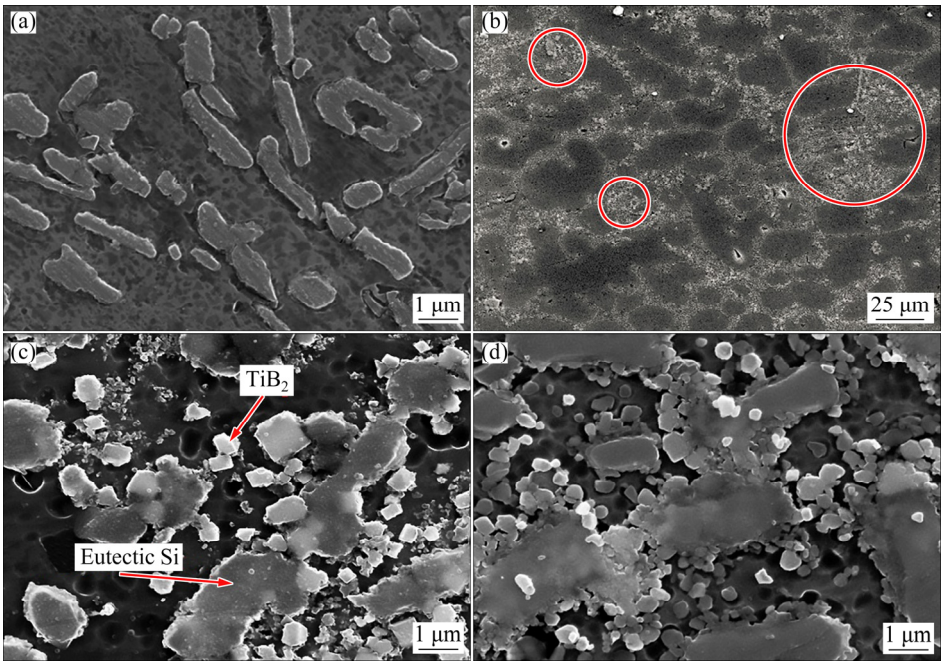

Fig. 4 Second electron micrographs of Al−7Si−0.3Mg alloy (a) and in-situ TiB_2/Al−7Si−0.3Mg composite (b−d) showing evolution of eutectic Si by introducing TiB_2 particles

the as-cast in-situ composites [35]. Although there is no consensus on the cause of aggregation, it is generally known that the TiB_2 clusters are mainly caused by reaction of by-products [36], such as Al_3Ti and reactive elements (e.g. K) [37], as well as the particle pushing of solidification front [38]. Additionally, the agglomeration of TiB_2 particles is generally trapped between branches at the grain boundaries. REZAEI and HOSSEINI [33] reported that the possible reason was that the solidification occurred from the center to the periphery due to the mismatch of the thermal expansion coefficient between ceramic particles and substrate. This uneven solidified structure results in tiny TiB_2 being pushed to the inter-dendrite region by the solidification front. The average porosity of the TiB_2/Al−7Si−0.3Mg composite is 0.93% by drainage method, which is consistent with the fact that a large number of pores are not observed in the SEM images.

According to the heterogeneous nucleation theory and the result of FAN et al [39], a monoatomic layer of Al_3Ti was adsorbed by the Al−Ti melt on the surface of in-situ TiB_2 particles, which significantly enhanced the effectiveness of TiB_2 particles for α(Al) nucleation. Figure 5 shows the EBSD results and statistical distributions of grain size of the Al−7Si−0.3Mg alloy and the TiB_2/Al−7Si−0.3Mg composite at the same magnification. It is seen that the Al−7Si−0.3Mg alloy is composed of coarse columnar α(Al) grains. However, the grains are highly refined through the heterogeneous nucleation of TiB_2 and appear as isometric crystals.

The SEM image and EDS spectra of the TiB_2/Al−7Si−0.3Mg composite are shown in Fig. 6. Since the TiB_2 accounts for only 2 vol.% in the present composites, B showed a weak distribution in the EDS spectrum. There are only Al, Si and TiB_2 in the material based on the previous XRD results. The distributions of Ti and Si elements verified that the TiB_2 particles mainly co-existed with the eutectic Si at the grain boundaries.

Figure 7 exhibits the results of the in-situ TiB_2/Al−7Si−0.3Mg samples by electron probe microscopy and backscatter imaging. From Fig. 7, it can be concluded that under backscatter imaging, the Bragg conditions change due to the presence of TiB_2 particles. Thereby different contrasts are displayed in the image, in which the Al−Si matrix is a dark image, and the TiB_2 particles appear as brighter small spots.

Furthermore, TEM was used to investigate the combination and homogeneity of TiB_2 particles. The TEM images of the in-situ TiB_2/Al−7Si−0.3Mg composite are shown in Fig. 8. Figure 8(a) shows that the TiB_2 in agglomeration or single particle is tightly bound to the matrix. In Figs. 8(a−c), most

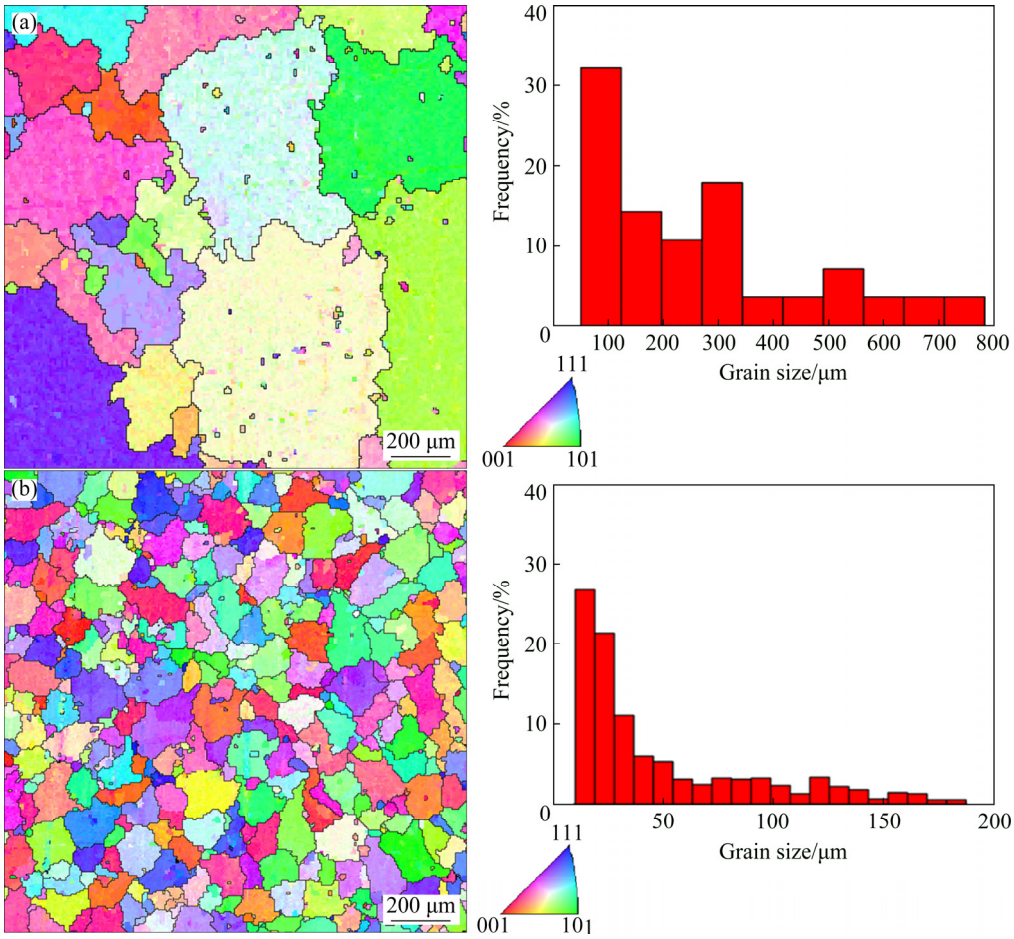

Fig. 5 EBSD results and grain size distributions of Al−7Si−0.3Mg alloy (a) and in-situ TiB_2/Al−7Si−0.3Mg composite (b)

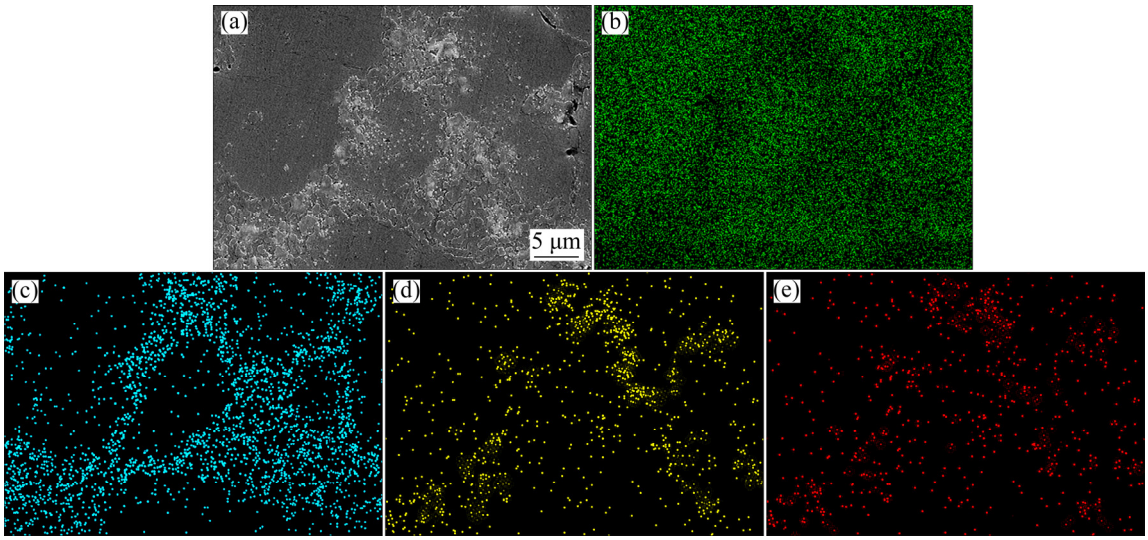

Fig. 6 SEM image (a) and EDS spectra of in-situ TiB_2/Al−7Si−0.3Mg composite showing distributions of Al (b), Si (c), Ti (d) and B (e)

TiB_2 particles are demonstrated as single particle with group overlap. The size of the TiB_2 particles is within the scope of 20−80 nm. For these nondeformable TiB_2 particles, the dislocation will be subjected to the combined effect of repulsive particle force and external shear stress during the

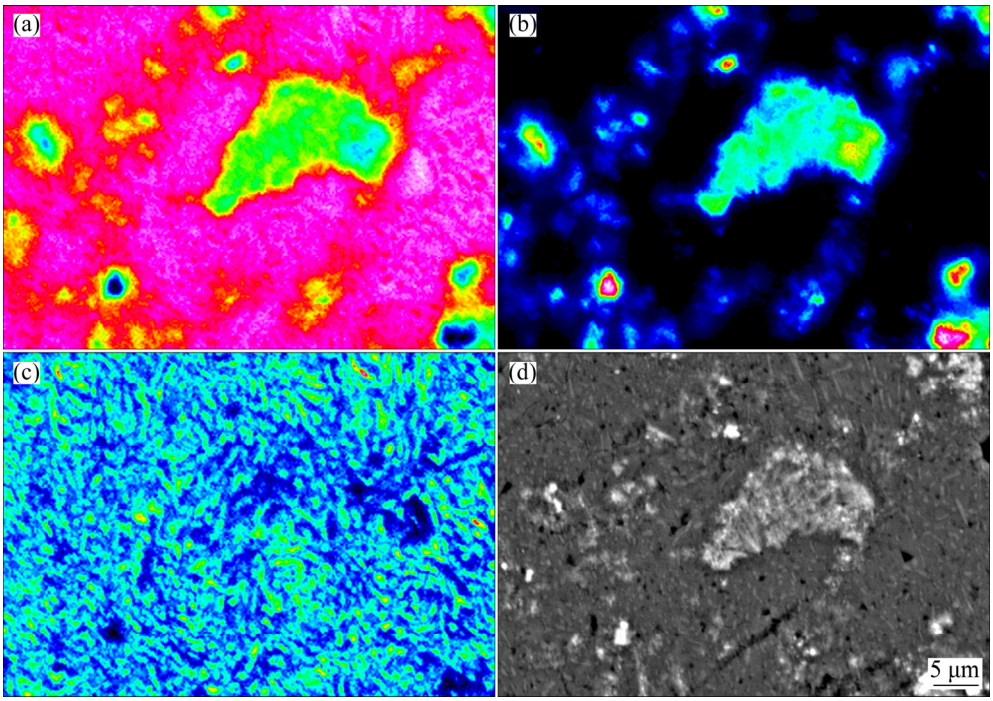

Fig. 7 EPMA images showing distributions of Al (a), Ti (b), Si (c), and backscattered electron image (d) of in-situ TiB_2/Al−7Si−0.3Mg composite

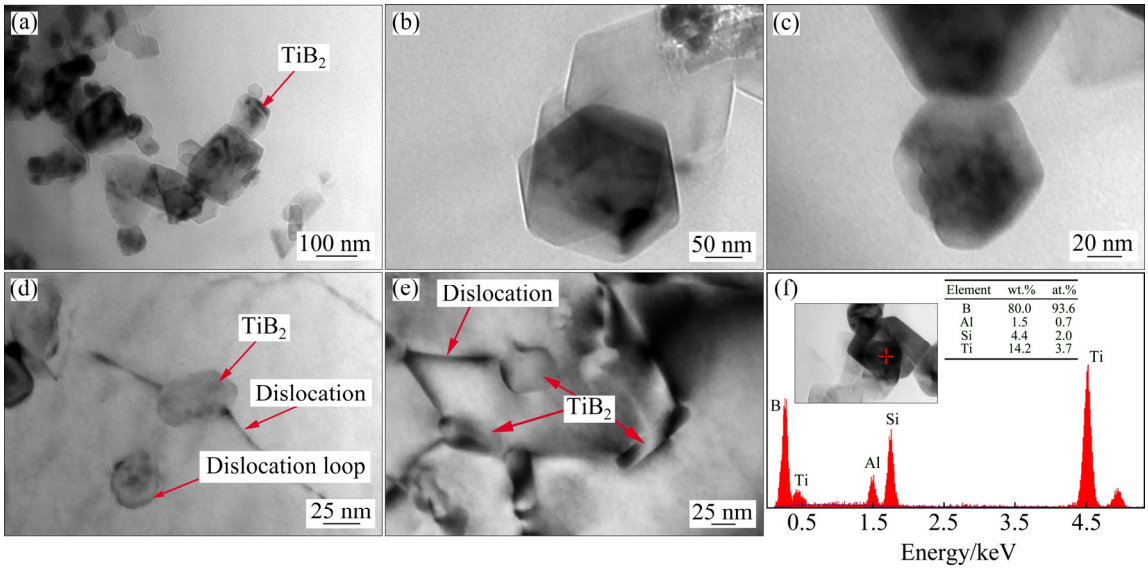

Fig. 8 Morphologies of in-situ TiB_2 particles at different magnifications (a−c), interaction between TiB_2 particles and dislocations (d, e), and EDS result (f)

stretch, which causes the dislocation to bypass the particles and leave a dislocation loop around the particles. The dislocation loop left by the dislocations around the particles is shown in Fig. 8(d). Generally, the particle size should be smaller than 1 μm to initiate this strengthening mechanism (Orowan strengthening) [40].

Additionally, EDS results are shown in Fig. 8(f), indicating that the micro-region contains Ti, B, Si, and Al elements, which can be confirmed as TiB_2 nano-particles. It is also found that the intensity of B is eminent, and its molar fraction exceeds 90%. The results detected by EDS from the light elements (from Be to N) sometimes seriously deviate from the actual contents, which have no referential significance to quantitative analysis but could reliably provide evidence of the existence of B element.

Tensile stress−strain curves of the Al−7Si−0.3Mg alloy and the in-situ TiB_2/Al−7Si−0.3Mg composite at room temperature are shown in Fig. 9, and the yield strength and ultimate tensile strength are listed in Table 2. The strengthening mechanisms introduced by nano TiB_2 particles including grain refinement strengthening (Hall−Petch relation), load-bearing strengthening (strong interfacial bonding between the nano-particles and the matrix), CTE mismatch strengthening, and Orowan strengthening [41−43].

The SEM images of tensile fracture surfaces of the Al−7Si−0.3Mg alloy and the in-situ TiB_2/Al−7Si−0.3Mg composite are shown in Fig. 10. It is seen from Fig. 10(a) that the fracture surface of the Al−7Si−0.3Mg alloy is mixed with brittle fracture and plastic fracture. Many tearing ribs and deep dimples on the fracture surface can be observed, legibly scrutinized in the enlarged view of the area in Fig. 10(b). At the same time, a small number of flat quasi-dissociation planes are also observed. Since the Al matrix has a face-centered cubic structure, there is substantially no dissociation fracture. Therefore, it can be concluded that quasi-dissociation is the main fracture form of the Al−7Si−0.3Mg alloy. The long strip-shaped eutectic Si phase is hard and brittle and has a great difference from the matrix deformation. When the tensile pressure is applied, the eutectic Si, especially at the end of sharp points, generates a large stress concentration and crack, which is caused by stretching. When the crack grows, the adjacent microcracks become larger cracks, and there is also a small brittle phase in the matrix [44].

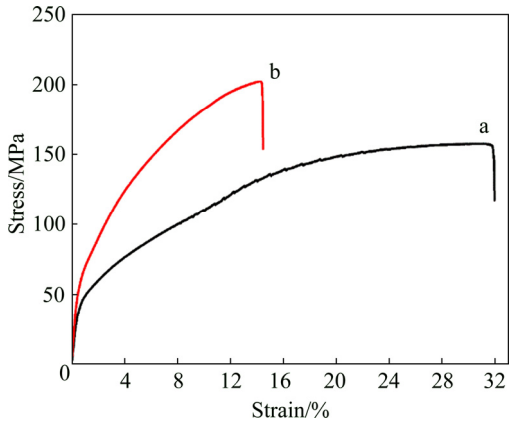

Fig. 9 Tensile stress−strain curves of Al−7Si−0.3Mg alloy (a) and in-situ TiB_2/Al−7Si−0.3Mg composite (b)

Table 2 Yield strength and ultimate tensile strength of Al−7Si−0.3Mg alloy and in-situ TiB_2/Al−7Si−0.3Mg composite at room temperature

Material	Yield strength/MPa	Ultimate tensile strength/MPa
Al−7Si−0.3Mg	40.76	157.56
TiB_2/Al−7Si−0.3Mg	54.99	202.15

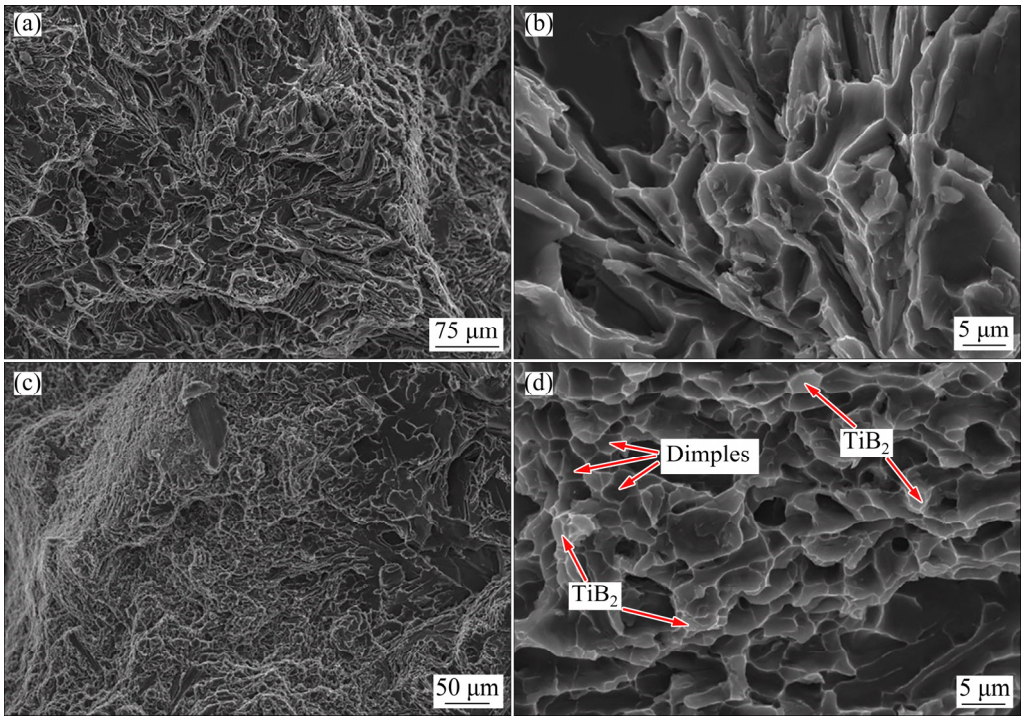

Fig. 10 SEM images of tensile fracture surfaces of Al−7Si−0.3Mg alloy (a, b) and in-situ TiB_2/Al−7Si−0.3Mg composite (c, d) (The dimples and TiB_2 reinforcement particles are indicated by arrows)

Figure 10(c) shows SEM image of the tensile fracture surface of the agglomerated portion of TiB_2 particles in the in-situ TiB_2/Al−7Si−0.3Mg composite. It is seen that the agglomerated portion of the left side has a significant difference from that of the right side. There is a clear quasi-dissociation plane on the right side, but many small and shallow equiaxed dimples appear on the left side. The enlarged view of Fig. 10(c) is shown in Fig. 10(d). This phenomenon is related to the small size and dense distribution of the TiB_2 particles, as well as the refinement of Si particles.

3.3 Microstructure and mechanical properties of Al−*x*Si−0.3Mg alloys and TiB_2/Al−*x*Si−Mg composites

Figure 11 shows the SEM images of the Al−*x*Si−0.3Mg alloys and the in-situ TiB_2/Al−*x*Si−0.3Mg composites. Compared with the matrix alloys, the eutectic Si in the composites changes from a dendritic shape to an equiaxed shape. This microstructural characteristic results from the high elastic modulus (550 GPa) and uniform distribution of the TiB_2. Besides, TiB_2 and α(Al) have a partially coherent relationship, and the TiB_2 particles affect the nucleation and growth of α(Al). The base or core of heterogeneous nucleation can refine the grain of α(Al) and change the growth mode of α(Al) grain from dendritic growth to chrysanthemum growth or equiaxed growth, which is conducive to the rigidity of the composites and leads to a higher strength of the composites.

Tensile stress−strain curves of the Al−*x*Si−0.3Mg alloys and the in-situ TiB_2/Al−*x*Si−0.3Mg composites at room temperature are shown in Fig. 12. The corresponding tensile strength and

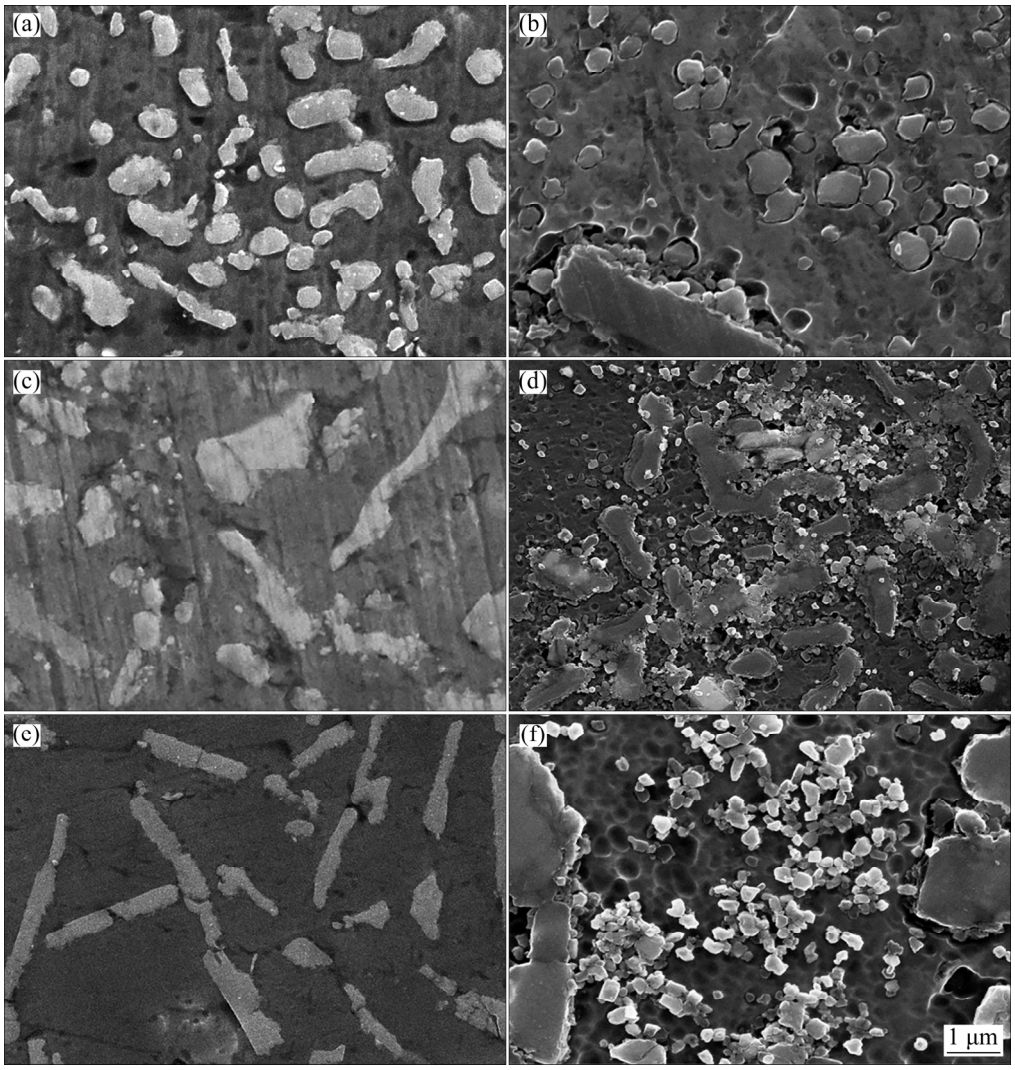

Fig. 11 SEM images of Al−*x*Si−0.3Mg alloys (a, c, e) and in-situ TiB_2/Al−*x*Si−0.3Mg composites (b, d, f): (a, b) *x*=9; (c, d) *x*=12; (e, f) *x*=15

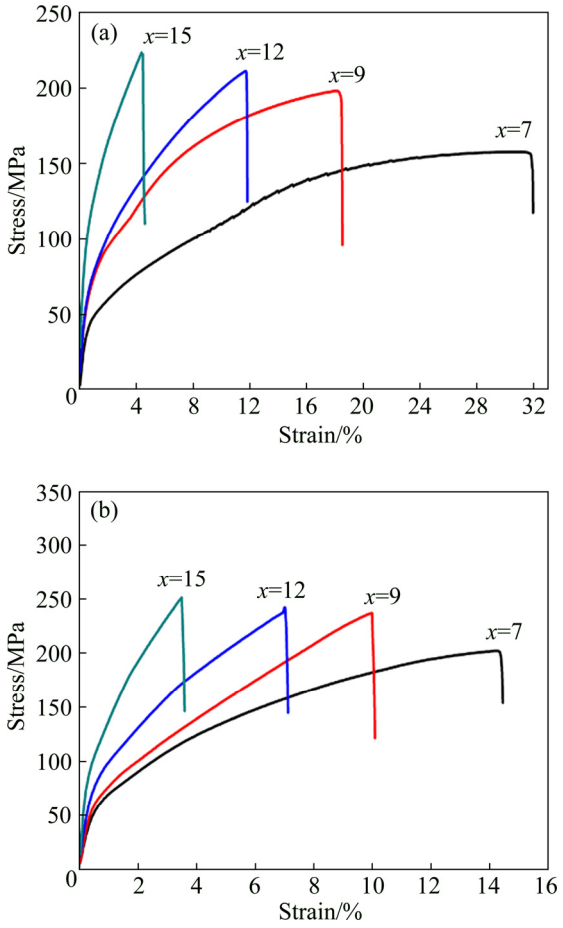

Fig. 12 Tensile stress−strain curves of Al−*x*Si−0.3Mg alloys (a) and in-situ TiB_2/Al−*x*Si−0.3Mg composites (b)

elongation are illustrated in Table 3. It is seen that the strength of the matrix alloy is improved gradually with the increase of Si content, but the elongation is reduced at the same time. With introducing the TiB_2 particles, the overall strength of the composites is enhanced significantly, which is similar to the influence of Si content on the matrix alloy. With increasing Si content, the tensile strength of TiB_2/Al−*x*Si−0.3Mg composites increases and the elongation decreases, which indicates that the Si phases strengthens the matrix but reduces the plasticity. The mechanism of plasticity reduction has been discussed in the previous Al−7Si−0.3Mg part. This result shows that the in-situ TiB_2 particles also contribute to the strength of the composites, even with higher Si contents.

Figure 13 shows the evolution of Brinell hardness (HB) of the Al−*x*Si−0.3Mg alloys and the TiB_2/Al−*x*Si−0.3Mg composites. It is seen that the overall hardness of the composites is higher than that of the matrix alloys. The hardness of the TiB_2/Al−7Si−0.3Mg composite increases from HB 48.18 (for Al−7Si−0.3Mg alloy) to HB 59.76. Therefore, the hardness of the alloy material can be improved by the in-situ TiB_2 particles. This phenomenon is also similar to that reported in the TiB_2/Al−7Si−0.3Mg composite.

SEM images of tensile fracture surfaces of the in-situ TiB_2/Al−*x*Si−0.3Mg composites are shown in Fig. 14. With the increase of Si content, the brittle characteristics (such as river patterns and crystal fractures) are more evident. Noticeable tearing edges are also observed, indicating the plasticity of the composites. There are apparent steps and cleavage planes in the TiB_2/Al−9Si−0.3Mg composite, and some dimples and serpentine slips are also observed, as shown in Fig. 14(a). The cleavage plane results from the cleavage of materials and a family of parallel crystal planes (all cleavage planes) under the tensile stress. For the TiB_2/Al−12Si−0.3Mg composite, as shown in Fig. 14(b), many intergranular fractures are predominant, accompanied by some dimples and tear edges. The increase of Si content reduces the grain boundary bonding strength. However, in some areas, the TiB_2 particles consume much energy during deformation due to the refinement of Si particles. Therefore, the fracture morphology of the TiB_2/Al−12Si−0.3Mg composite shows tearing

Table 3 Ultimate tensile strength and elongation of Al−*x*Si−0.3Mg alloys and in-situ TiB_2/Al−*x*Si−0.3Mg composites at room temperature

x	Ultimate tensile strength/MPa		Elongation/%	
	Al−*x*Si−0.3Mg	TiB_2/Al−*x*Si−0.3Mg	Al−*x*Si−0.3Mg	TiB_2/Al−*x*Si−0.3Mg
7	157.56	202.15	29.70	12.51
9	198.08	236.72	16.15	8.47
12	211.10	241.90	10.21	5.61
15	223.45	251.11	3.38	2.83

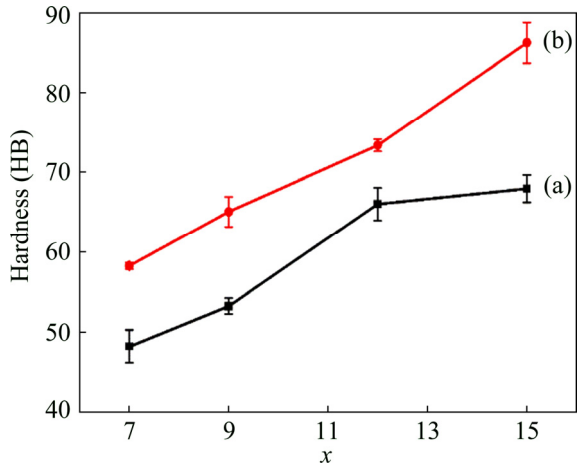

Fig. 13 Brinell hardness of Al−*x*Si−0.3Mg alloys (a) and in-situ TiB_2/Al−*x*Si−0.3Mg composites (b)

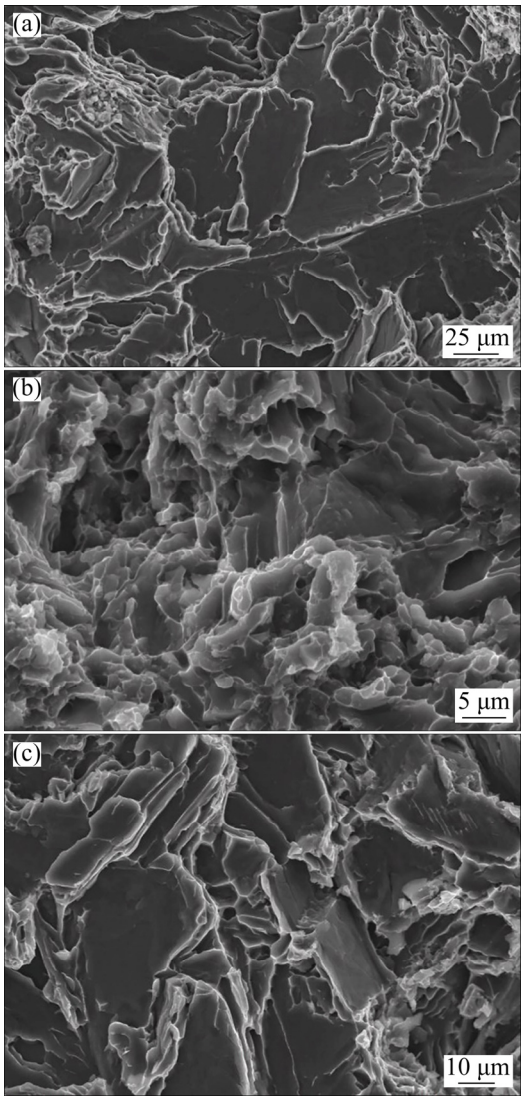

Fig. 14 SEM images of tensile fracture surfaces of in-situ TiB_2/Al−*x*Si−0.3Mg composites: (a) *x*=9; (b) *x*=12; (c) *x*=15

edges with good toughness. For the TiB_2/Al−15Si−0.3Mg composite, as shown in Fig. 14(c), the fracture surface is quite different from that of the above mentioned two composites. The cleavage cracks are observed, suggesting the increased brittleness of the composite. Generally, the plasticity of the TiB_2/Al−*x*Si−0.3Mg composites decreases sharply with the increase of Si content, but the refining effect of TiB_2 particles on the Si phase is favorable for plasticity. Therefore, the overall strength of the composites increases, but the plasticity decreases, while a part of the toughness remains. The interaction between the in-situ TiB_2 particles and the Si phase may be a solution to solve the problem of low plasticity of Al−Si alloys with a high Si content.

4 Conclusions

(1) In-situ TiB_2/Al−*x*Si−0.3Mg composites are prepared by the mixed salt−metal reaction, and the porosity of the composites is approximately 0.93%.

(2) In the TiB_2/Al−7Si−0.3Mg composite, the TiB_2 particles with a diameter of 20−80 nm and the eutectic Si phase with a length of 1−10 μm are observed. The TiB_2 particles hinder the growth of matrix grains, resulting in an evident grain boundary pinning effect and changing the eutectic Si phase from long needle shape to short-rod shape.

(3) Compared with those of the Al−*x*Si−0.3Mg alloys, the mechanical properties of the TiB_2/Al−*x*Si−0.3Mg composites are improved while maintaining certain plasticity. The tensile strength and Brinell hardness of the TiB_2/Al−7Si−0.3Mg composites increase from 157.56 MPa, HB 48.18 to 202.15 MPa, HB 59.76, respectively, compared with those of Al−7Si−0.3Mg alloy.

(4) A quasi-cleavage dominated fracture is the major fracture mode of the Al−*x*Si−0.3Mg alloys, while there are more brittle fracture modes in the TiB_2/Al−*x*Si−0.3Mg composites.

Acknowledgments

The authors are grateful for the financial supports from the National Natural Science Foundation of China (51804349), the China Postdoctoral Science Foundation (2018M632986), and the Natural Science Foundation of Hunan Province, China (2019JJ50766).

References

[1] GOULART P R, SPINELLI J E, OSÓRIO W R, GARCIA A. Mechanical properties as a function of microstructure and solidification thermal variables of Al−Si castings [J]. Materials Science and Engineering A, 2006, 421: 245−253.

[2] NALLUSAMY S. A review on the effects of casting quality, microstructure and mechanical properties of cast Al−Si−0.3Mg alloy [J]. International Journal of Performability Engineering, 2016, 12: 143−154.

[3] IBRAHIM M F, ABDELAZIZ M H, SAMUEL A M, DOTY H W, SAMUEL F H. Effect of rare earth metals on the mechanical properties and fractography of Al–Si-based alloys [J]. International Journal of Metalcasting, 2020, 14: 108−124.

[4] ZHANG Wen-da, LIU Yun, YANG Jing, DANG Jin-zhi, XU Hong, DU Zhen-min. Effects of Sc content on the microstructure of as-cast Al−7wt.%Si alloys [J]. Materials Characterization, 2012, 66: 104−110.

[5] HU Zhi, YAN Hong, RAO Yuan-sheng. Effects of samarium addition on microstructure and mechanical properties of as-cast Al−Si−Cu alloy [J]. Transactions of Nonferrous Metals Society of China, 2013, 23: 3228−3234.

[6] HARO-RODRÍGUEZ S, GOYTIA-REYES R E, DWIVEDI D K, BALTAZAR-HERNÁNDEZ V H, FLORES-ZÚÑIGA H, PÉREZ-LÓPEZ M J. On influence of Ti and Sr on microstructure, mechanical properties and quality index of cast eutectic Al−Si−Mg alloy [J]. Materials & Design, 2011, 32: 1865−1871.

[7] CAO F Y, JIA Y D, PRASHANTH K G, MA P, LIU J S, SCUDINO S, HUANG F, ECKERT J, SUN J F. Evolution of microstructure and mechanical properties of as-cast Al−50Si alloy due to heat treatment and P modifier content[J]. Materials & Design, 2015, 74: 150−156.

[8] LI Bao, WANG Hong-wei, JIE Jin-chuan, WEI Zun-jie. Effects of yttrium and heat treatment on the micro-structure and tensile properties of Al−7.5Si−0.5Mg alloy [J]. Materials & Design, 2011, 32: 1617−1622.

[9] SUN Jing, ZHANG Xiao-bo, ZHANG Yi-jie, MA Nai-heng, WANG Hao-wei. Modification mechanism of primary silicon by TiB_2 particles in a TiB_2/ZL109 composite [J]. Journal of Materials Science, 2014, 50: 1237−1247.

[10] ALANEME K K, BODUNRIN M O. Corrosion behavior of alumina reinforced aluminum (6063) metal matrix composites [J]. Journal of Minerals & Materials Characterization & Engineering, 2011, 10: 1153−1165.

[11] FATHY A, SHEHATA F, ABDELHAMEED M, ELMAHDY M. Compressive and wear resistance of nanometric alumina reinforced copper matrix composites [J]. Materials & Design, 2012, 36: 100−107.

[12] YI Hong-zhan, MA Nai-heng, LI Xian-feng, ZHANG Yi-jie, WANG Hao-wei. High-temperature mechanics properties of in-situ TiB_2 reinforced Al−Si alloy composites [J]. Materials Science and Engineering A, 2006, 419: 12−17.

[13] LLOYD D J. Particle reinforced aluminium and magnesium matrix composites [J]. Metallurgical Reviews, 1994, 39: 1−23.

[14] CAO X, CAMPBELL J. Oxide inclusion defects in Al−Si−Mg cast alloys [J]. Canadian Metallurgical Quarterly, 2005, 44: 435−448.

[15] GOTMAN I, KOCZAK M J, SHTESSEL E. Fabrication of Al matrix in situ composites via self-propagating synthesis [J]. Materials Science and Engineering A, 1994, 187: 189−199.

[16] CLYNE T W, ROBERT M H. Stability of intermetallic aluminides in liquid aluminium and implications for grain refinement [J]. Metals Technology, 1980, 7: 177−185.

[17] SINGH H, RAINA A, IRFAN M. Effect of TiB_2 on mechanical and tribological properties of aluminum alloys—A review [J]. Materials Today: Proceedings, 2018, 5: 17982−17988.

[18] CHANDANA A, LAWRENCE I D, JAYABAL S. Characterization of particulate-reinforced aluminium 7075/TiB_2 composites [J]. Materials Today: Proceedings, 2018, 5: 14317−14326.

[19] SINGH R K, TELANG A, DAS S. Microstructure, mechanical properties and two-body abrasive wear behaviour of hypereutectic Al−Si−SiC composite [J]. Transactions of Nonferrous Metals Society of China, 2020, 30: 65−75.

[20] NIMBALKAR V M, PANDAV S G, MOHAPE M R, DESHMUKH V P, DEOLE S, TAMBAVEKAR A S, BAVISKAR V R, SABLE S R, CHITALE M M. Development of novel Al-alloy (Al−5Mg)/10wt.%TiB_2 metal matrix composites by in situ reaction synthesis [J]. Materials Science Forum, 2015, 830−831: 460−462.

[21] WANG Ming-liang, CHEN Dong, CHEN Zhe, WU yi, WANG Fei-fei, MA Nai-heng, WANG Hao-wei. Mechanical properties of in-situ TiB_2/A356 composites [J]. Materials Science and Engineering A, 2014, 590: 246−254.

[22] PRADEEP K G S, KESHAVAMURTHY R, KUPPAHALLI P, KUMARI P. Influence of hot forging on tribological behavior of Al6061−TiB_2 in-situ composites [J]. IOP Conference Series: Materials Science and Engineering, 2016, 149: 012087.

[23] PRAMOD S L, BAKSHI S R, MURTY B S. Aluminum-based cast in situ composites: A review [J]. Journal of Materials Engineering and Performance, 2015, 24(6): 2185−2207.

[24] LI S F, KONDOH K, IMAI H, CHEN B, JIA L, UMEDA J, FU Y B. Strengthening behavior of in situ-synthesized (TiC−TiB)/Ti composites by powder metallurgy and hot extrusion [J]. Materials & Design, 2016, 95: 127−132.

[25] GENG Ji-wei, LIU Gen, HONG Tian-ran, WANG Ming-liang, CHEN Dong, MA Nai-heng, WANG Hao-wei. Tuning the microstructure features of in-situ nano TiB_2/Al−Cu−Mg composites to enhance mechanical properties [J]. Journal of Alloys and Compounds, 2019, 775: 193−201.

[26] SU Jie, LI Ya-zhi, JIANG Wei, ZHANG Da-long. Study on microscopic ductile fracture of in-situ TiB_2/2024 Al matrix composite [J]. Procedia Structural Integrity, 2016, 2: 2222−2229.

[27] ZHANG L L, JIANG H X, HE J, ZHAO J Z. Kinetic behaviour of TiB_2 particles in Al melt and their effect on grain refinement of aluminium alloys [J]. Transactions of Nonferrous Metals Society of China, 2020, 30: 2035−2044.

[28] VIVEKANANDA A S, PRABU S B, PASKARA-

MOORTHY R. Influence of process parameters of aluminothermic reduction process on grain refinement of in-situ Al/TiB_2 composites [J]. Materials Today: Proceedings, 2018, 5:1071−1075.

[29] JAVADI A, PAN S H, LI X C. Fabrication of high strength Al nanocomposites with populous TiB_2 nano-particles [J]. Procedia Manufacturing, 2018, 26: 629−632.

[30] RAJAN H B M, RAMABALAN S, DINAHARAN I, VIJAY S J. Synthesis and characterization of in situ formed titanium diboride particulate reinforced AA7075 aluminum alloy cast composites [J]. Materials & Design, 2013, 44: 438−445.

[31] RAJAN H B M, DINAHARAN I, RAMABALAN S, AKINLABI E T. Influence of friction stir processing on microstructure and properties of AA7075/TiB_2 in situ composite [J]. Journal of Alloys and Compounds, 2016, 657: 250−260.

[32] FENG C F, FROYEN L. Microstructures of in situ Al/TiB_2 MMCs prepared by a casting route [J]. Journal of Materials Science, 2000, 35(4): 837−850.

[33] REZAEI A, HOSSEINI H R M. Evolution of microstructure and mechanical properties of Al−5wt%Ti composite fabricated by P/M and hot extrusion: Effect of heat treatment [J]. Materials Science and Engineering A, 2017, 689: 166−175.

[34] MALCOLM W, CHASE J. NIST-JANAF thermochemical tables fourth edition [M]. 4th ed. New York: American Institute of Physics and the American Chemical Society, 1998.

[35] ZHANG S L, SHI X X, ZHAO Y T, ZHANG B G, LIANG Z P, YIN H S, DOU B Y, ZHANG Q L, WANG C X. Preparation, microstructures and mechanical properties of in-situ (TiB_2+ZrB_2)/$AlSi_9Cu_3$ composites [J]. Journal of Alloys and Compounds, 2016, 673: 349−357.

[36] WATSON I G, FORSTER M F, LEE P D, DASHWOOD R J, HAMILTON R W, CHIRAZI A. Investigation of the clustering behaviour of titanium diboride particles in aluminium [J]. Composites Part A: Applied Science and Manufacturing, 2005, 36: 1177−1187.

[37] LÜ L, LAI M O, SU Y, TEO H L, FENG C F. In situ TiB_2 reinforced Al alloy composites [J]. Scripta Materialia, 2001, 45: 1017−1023.

[38] SCHAFFER P L, MILLER D N, DAHLE A K. Crystallography of engulfed and pushed TiB_2 particles in aluminium [J]. Scripta Materialia, 2007, 57(12): 1129−1132.

[39] FAN Z Y, WANG Y, ZHANG Y J, QIN T, ZHOU X R, TOMPSON G E, PENNYCOOK T, HASHIMOTO T. Grain refining mechanism in the Al/Al−Ti−B system [J]. Acta Materialia, 2015, 84: 292−304.

[40] ZADEH A S. Comparison between current models for the strength of particulate-reinforced metal matrix nanocomposites with emphasis on consideration of Hall−Petch effect [J]. Materials Science and Engineering A, 2012, 531: 112−118.

[41] KIM C S, SOHN I, NEZAFATI M, FERGUSON J B, SCLULTZ B F, GOHARI Z B, ROHATGI P K, CHO K. Prediction models for the yield strength of particle-reinforced unimodal pure magnesium (Mg) metal matrix nanocomposites (MMNCs) [J]. Journal of Materials Science, 2013, 48(12): 4191−4204.

[42] CHEN L Y, XU J Q, CHOI H, POZUELO M, MA X L, BHOWMICK S, YANG J M, MATHAUDHU S, LI X C. Processing and properties of magnesium containing a dense uniform dispersion of nano-particles [J]. Nature, 2015, 528(7583): 539−543.

[43] LIU G, ZHANG G J, JIANG F, DING X D, SUN Y J, MA E. Nanostructured high-strength molybdenum alloys with unprecedented tensile ductility [J]. Nature Materials, 2013, 12(4): 344−350.

[44] WANG Q G, CACERES C H, GRIFFITHS J R. Damage by eutectic particle cracking in aluminum casting alloys A356/357 [J]. Metallurgical and Materials Transactions A, 2003, 34: 2901−2912.

原位 TiB_2/Al−*x*Si−0.3Mg 复合材料的显微组织与力学性能

刘宇轩[1]，王日初[1,2]，彭超群[1]，蔡志勇[1,2]，周朝晖[3]，李晓庚[3]，曹玄扬[3]

1. 中南大学 材料科学与工程学院，长沙 410083；
2. 中南大学 轻质高强结构材料国防科技重点实验室，长沙 410083；
3. 长沙新材料产业研究院，长沙 410000

摘　要：采用盐−金属反应制备原位 2% TiB_2(体积分数)颗粒增强 Al−*x*Si−0.3Mg(*x*=7%, 9%, 12%, 15%，质量分数)复合材料，并对其显微组织和力学性能进行研究。结果表明，TiB_2/Al−*x*Si−0.3Mg 复合材料中的主要强化相是直径为 20~80 nm 的 TiB_2 颗粒和长度为 1~10 μm 的共晶硅相。TiB_2 颗粒能促进晶粒细化，使共晶硅由针状变为短棒状。但是，当 Si 含量超过共晶成分时，TiB_2 颗粒的强化作用减弱，这可能是由于形成了大且不规则的初生 Si 相。轴向拉伸试验和断裂观察结果表明，复合材料比相同成分的基体合金具有更多的脆性断裂特征。

关键词：铝硅合金；原位反应；铝基复合材料；显微组织；力学性能

(Edited by Wei-ping CHEN)